Orographic and convective gravity waves above the Alps and Andes mountains during GPS radio occultation events – a case study

5   Rodrigo Hierro[1], Andrea K. Steiner[2], Alejandro de la Torre[1], Peter Alexander[3], Pablo Llamedo[1], Pablo Cremades[4]

Correspondence to: Rodrigo Hierro (rhierro@austral.edu.ar)

[1] Facultad de Ingeniería, Universidad Austral and CONICET, Pilar, Provincia de Buenos Aires
10   B1629ODT, Argentina

[2] Wegener Center for Climate and Global Change (WEGC) and Institute for Geophysics, Astrophysics, and Meteorology/Institute of Physics, University of Graz, Graz, Austria

[3] IFIBA, CONICET, Ciudad Universitaria, Buenos Aires, Argentina

[4] Facultad de Ciencias Exactas y Naturales, Universidad Nacional de Cuyo, Argentina

Abstract. Gravity waves (GW) and convective systems play a fundamental role in atmospheric circulation, weather, and climate. The main sources of GW are orographic effects triggering mountain
20   waves and convective activity. We test the utility of Global Positioning System (GPS) radio occultation (RO) observations for the investigation of convective systems and GW over orographic regions in Europe and South America. We build a collocation database between RO events and convective systems over sub-tropical to mid-latitude mountain regions close to the Alps and Andes. Subsets of RO profiles are sampled and a case study is selected for each region. From mesoscale numerical simulations, we analyze
25   relevant gravity waves features (main parameters, generation and propagation), mainly from orographic and convective activity origin for the case studies considered. Similar GW regimes and dominant vertical and horizontal wavelengths, from convective and orographic sources, are found in both regions. Mountain waves above the Alps are found to reach higher altitudes than close to the Andes, as the background subtropical jet above this region constrains the propagation of GW packets up to stratospheric heights.
30   From recent results, the distortion introduced in the measured atmospheric vertical gravity wavelength by one of the RO events is illustratively discussed. In our analysis we take into account both the elevation angle of the sounding path (line of tangent points) and the gravity wave aspect ratio estimated from the simulations and the line of sight. In both case studies, a considerable distortion and underestimation of the vertical wavelengths measured by RO may be expected.

1. Introduction

35

The Global Positioning System (GPS) radio occultation (RO) technique has been proven to be a powerful tool to analyze meteorological tropospheric features with a moderate/high spatial and temporal resolution in essentially any meteorological condition. Its ability to penetrate clouds allows to retrieve temperature (T) and water vapor pressure (e), amongst several other atmospheric variables with high vertical

40 resolution close to the near surface. Vertical profiles of T are provided with an accuracy of less than 1 K (e.g., Kursinski et al., 1997; Steiner and Kirchengast, 2005; Scherllin-Pirscher et al., 2011; 2017) in the troposphere to lower stratosphere and specific humidity with an accuracy of about 0.3 g kg^{-1} to 0.1 g kg^{-1} in the lower to middle troposphere (Kursinski and Gebhardt, 2014). Although measurements are taken irregularly in time and space, they provide a global coverage. Data are available from several missions

45 such as the CHAllenging Minisatellite Payload (CHAMP), Satélite deAplicaciones Científicas-C (SAC-C), Gravity Recovery and Climate Experiment (GRACE), or the Formosa Satellite mission-3/ Constellation Observing System for Meteorology, Ionosphere, and Climate mission (hereafter referred to as COSMIC), and found to be of high quality and consistency in the troposphere to lower stratosphere (e.g., Steiner et al., 2011; 2013; Angerer et al., 2017, this AMT special issue).

50 Biondi et al. (2011) recognized double tropopause events using bending angle (*BA*) anomalies derived from GPS RO measurements from different missions. Later, Biondi et al. (2014) found that the GPS RO technique is useful for understanding the thermal structure of tropical cyclones and possible overshootings into the stratosphere. The complexity of the relationship between deep convection and flow convergence over mountains has been widely studied. Demko et al. (2009) showed that during days with

55 deep convection, the convergence over mountains is weaker than on days when deep convection does not occur.

Over the Alps, considering the kinematic and dynamic features of divergence, flow splitting, or mesoscale vortices, it is possible to find regions which initiate or intensify the storms (Bica et al., 2007). Thermally driven flows over the Alps are associated to convergence caused by large-scale topographic heat flow

60 (Langhans et al., 2011). These flows supply moisture from source regions close to the surface, which stimulates the initiation of deep convection (e. g. Barthlott et al., 2006). Gladich et al. (2011) mentioned that southward oriented reliefs receive more solar radiation, resulting in a warmer atmosphere in comparison with flat terrain. Also, the orography presents a negative energetic balance as compared to flat regions.

65 Extratropical regions in the Southern Hemisphere show strong wave activity close to the Andes and to the Antarctic Peninsula (e.g., Eckermann and Preusse, 1999; de la Torre et al., 2012; Hierro et al., 2013). The eastern side of the Andes at mid-latitudes between the subtropical and polar jets (Houze, 2012) is a natural laboratory for gravity waves (GW), in particular mountain waves (MW). The dynamic processes involved in convection over this region have been analysed, e.g., by de la Torre et al. (2004), who found

70 that anabatic winds act as triggering mechanism in the presence of moist enthalpy under unstable conditions. A relationship between MW and the development of deep convection was found by de la Torre et al. (2011). Through the design of several non-dimensional numbers related to storms development and MW energy, Hierro et al. (2013) found that MW are able to provide the necessary

energy to overcome a surface stable layer. Vertically propagating short-period GW strongly affect the
75   general circulation as well as the structure of the middle atmosphere (e.g., Dutta et al., 2009).

Convective activity is one of the most important sources of GW through the release of latent heat,
contributing to the interaction between waves and mean flow in the middle atmosphere (e.g., Alexander,
1995; Pandya and Alexander, 1999). When a convective cloud reaches the mean flow, waves which
propagate upstream are generated (Beres et al., 2002 and references therein). Convective instability, in
80   turn, yields oscillatory movements, which give place to GW that propagate vertically as a harmonic
oscillator (e.g., Fritts and Alexander, 2003). Several authors have analyzed the main mechanisms which
describe the possible sources of gravity waves generated by convection. In the "obstacle effect", the
background finds a barrier given by the convective flow (Clarke et al., 1986). Fovell et al. (1992),
proposed a mechanism where updrafts and downdrafts reach the tropopause, generating high-frequency
85   GW. Röttger (1991) studied penetrating cumulus convection which generates GW by transferring kinetic
energy from the troposphere to the lower stratosphere.

Evan et al. (2012) determined that the Weather Research and Forecasting (WRF) mesoscale model
(Skamarock et al., 2008) is able to simulate stratospheric GW, when it is run under actual boundary
conditions. It was also possible to resolve GW generated by convection in the tropics. Stephan and
90   Alexander (2014), in turn, showed that WRF physics parameterizations are not decisive to get good
results from GW simulations. From WRF simulations above the Southern Andes, de la Torre et al. (2012)
detected systematic large-amplitude, stationary, nonhydrostatic GW structures, forced by the mountains
up to the lower stratosphere and persisting for several hours. Their dominant modes were characterized by
horizontal wavelengths (λ_H) of around 50 km. The vertical wavelengths (λ_Z) were estimated to be
95   between 2 km and 11 km. Over the Andes region, de la Torre et al. (2011) detected two main modes of
mountain waves with large amplitude and high intrinsic frequency. Over the same region, Hierro et al.
(2013) found stationary modes with λ_H between 40 km and 160 km and λ_Z of around 7 km. De la Torre et
al. (2015), analyzing storms in the presence of MW, distinguished two different structures in vertical
wind simulations. Both of them seem to be fixed to the mountains, defining systematic updraft and
100   downdraft sectors. GW parameters were analyzed from band-pass and wavelet analysis, indicating for the
cases analyzed the presence of short λ_H and long λ_Z, as expected for high intrinsic period GW.

The motivation of the present work is two folded: First, to find a set of collocations among GPS RO *BA*
and *T* profiles and mesoscale sub-tropical convective systems under reasonable conditions of proximity in
space and time occurrence. We use this dataset to determine the vertical structures of these systems over
105   orographic regions (Alps and Andes). To detect the cloud top altitude from the RO profiles, we apply a
technique based in the anomay in the *BA*. Then, the GW structures are discussed from high resolution
mesoscale model simulations. The possible determination of GW parameters from GPS RO is discussed
in detail for two case studies. Sect. 2 outlines the RO data used and the methodology applied and
describes two subsets of RO events retrieved during convective activity close to Alps and Andes ranges.
110   In Sect. 3, one case study at each region is selected and relevant GW features are analyzed in relation to
the simulation and the measurement of both RO events. In Sect. 4, conclusions are given.

2. Data and methodology

The utility of RO observations for the investigation of convective systems (Biondi et al, 2012; 2015b) and GW over orographic regions in Europe and South America (Alps and Andes mountains) is tested. It is known that a sharp spike in RO *BA* is highly correlated to the top of the cloud, corresponding to anomalously cold temperatures within the cloud. Above the cloud, the temperature returns to background conditions, and a strong inversion appears above the cloud top. For usual tropospheric cloud tops, the *T* lapse rate within the cloud often approaches a moist adiabat, consistent with rapid undiluted ascent within the convective systems.

We built a collocation database between RO observations and meso-scale convective systems over sub-tropical to mid-latitude mountain regions. The selected regions for the Alps and Andes are [40°N to 55°N, 0°E to 20°E] and [20°S to 40°S, 60°W to 74°W], respectively (Fig. 1). We use RO data processed at the Wegener Center for Climate and Global Change (WEGC) with the Occultation Processing System (OPS) version 5.6 (Schwärz et al., 2016), based on excess phase and orbit data version 2010.2640 from the University Corporation for Atmospheric Research (UCAR) from the CHAMP, SAC-C, GRACE, and COSMIC missions. We analyse *BA* and *T* profiles which are available from near surface up to 40 km altitude with 100 m vertical sampling.
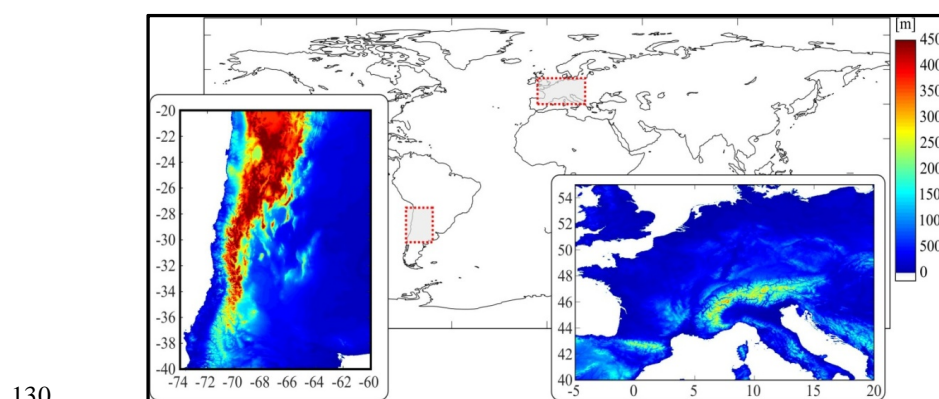
Figure 1: The Alps (right) and Andes (left) regions selected to build a collocation database between RO data and cloud data over sub-tropical to mid-latitude mountain regions.

Convective systems were located in time and space using the global deep convective tracking database of the International Satellite Cloud Climatology Project (ISCCP) (Rossow et al., 1996), from January 2006 to July 2008. This period was used due to the constraints in the ISCCP database, which is currently incomplete because it is being re-processed and data are only available for the present time period. The global data set with a horizontal grid resolution of 30 km and a nominal time resolution of 3 h is based on brightness temperatures from geostationary satellite measurements and provides information on the location and extent of mesoscale deep convective cloud systems and their properties.

The selection criterion applied in the present work considers the position of the RO observation with respect to the center of the storm and provides several case studies in each region. Accrding to this criterium, the latitude and longitude of the mean tangent point (MTP) belonging to each RO profile are taken within a radius of 100 km with respect to the center of the storm, as provided by ISCCP. A

145 maximum time interval of 3 h was allowed between each RO event and the data from ISCCP. The collocated events were checked using cloud data from geostationary satellites METEOSAT (Europe) and GOES (South America).

Collocated RO *BA* and *T* profiles were further used to determine the vertical structures of sub-tropical convective systems over orographic regions. In order to detect the cloud top altitude with RO, we applied

150 the anomaly technique developed by Biondi et al. (2013) for anomalous atmospheric profile and cloud top detection of convective systems. Each *BA* and *T* profile collocated with a storm was referenced against a RO background reference climatology profile, which was extracted for the same location and the same month from the global RO *BA* and *T* reference climatology, respectively (for details see Biondi et al. (2017)). We then subtracted the collocated RO reference climatology profile from the individual RO

155 profile. *BA* was normalized with respect to the reference climatology profile in order to obtain a fractional anomaly profile. The cloud top altitude is represented as a pronounced spike in the vertical *BA* anomaly structure, and correspondingly in the *T* anomaly profile.

GW were also analyzed using WRF mesoscale simulations, performed using 1°×1° National Center of Enviromental Prediction (NCEP) Global Final Analysis (FNL), as boundary conditions. They are

160 conducted in four nested domains (27 km, 9 km, 3 km, and 1 km respectively) with 50 vertical levels. A sponge layer was applied in the upper 3 km. The size of the inner domain in the Alps region is about 300 km x 200 km and that of the Andes region about 300 km x 300 km. For each domain, the microphysical schemes used were the following: WRF Single Moment-6 class (WSM6; Hong et al., 2004); Yonsei University (YSU; Hong et al., 2006) to represent the planetary boundary-layer (PBL) physics; Rapid

165 Radiative Transfer Model Longwave (RRTM; Mlawer et al., 1997) and MM5 Dudhia Shortwave (Dudhia scheme; Dudhia, 1989) for radiation processes; the Noah land surface model (developed jointly by NCAR and NCEP; Skamarock et al., 2008) and Monin–Obukhov scheme; (Monin and Obukhov, 1954) for surface physics and thermal diffusion processes respectively. The cumulus parameterization used was the New Grell scheme (Grell3; (Grell and Devenyi, 2002)) for the first three domains, while no-cumulus

170 parameterization was selected for the inner one.

Five collocations were pre-selected in each region, with the aim of analyzing and comparing typical GW characteristics in the vicinity of both mountain ranges (Fig. 2). All of the pre-selected collocations show some spikes in the *BA* profile, of which one is correlated with the cloud top of the corresponding convective structure. Large amplitude oscillations that could be associated to hydrostatic GW propagation

175 are observed. We further focused on two representative case studies (central frames in upper and lower panels in Fig. 2). These exhibit interesting oscillatory features and correspond in the Alps region to 02 Feb 2008, 17:24 UTC (47.29°N, 12.02°W), and in the Andes region to 19 Dec 2006, 16:56 UTC (25.35°S, 67.37°W).

180
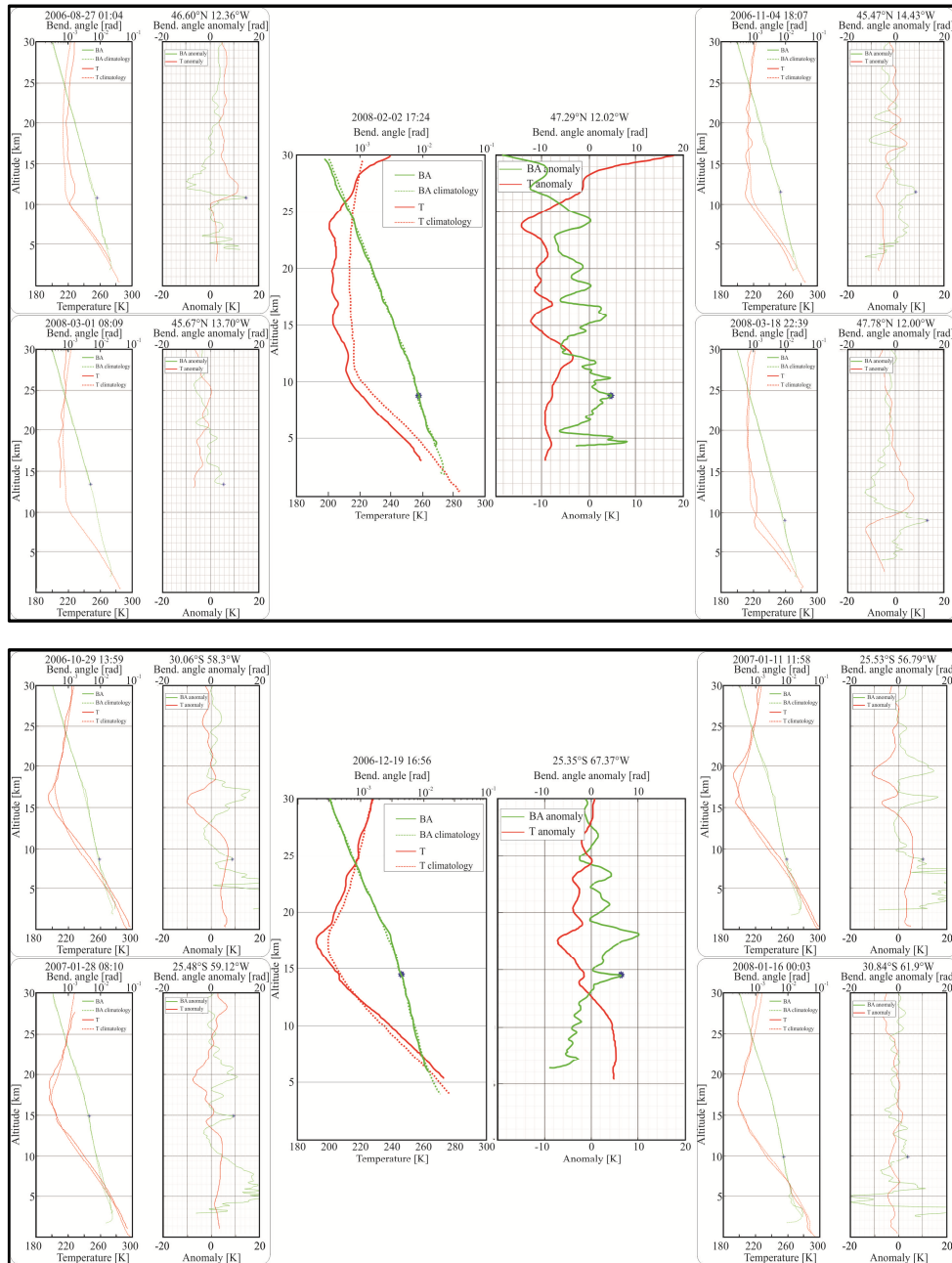
Figure 2: Pre-selected collocations between GPS RO profiles and convective developments in the Alps region (upper panels) and the Andes region (lower panels). Shown are absolute profiles and anomaly profiles for bending angle (green) and temperature (red), and the respective climatology profile (dotted).

185   The cloud top height is indicated by a blue star.

3. WRF model simulations and analyses of GPS RO observations

190   The two selected study cases for the Alps and Andes region were further closely investigated by means of numerical simulations with the WRF model and through gravity wave analysis of the GPS RO observational profiles.

3.1. Study case for the Alps region

195   *3.1.1. Numerical simulations of gravity wave structures*

For study case one in the Alps region, we simulated dynamic and thermodynamic parameters. In Fig. 3 we show the vertical air velocity (w) in the considered area at two altitude levels (8 km and 12.5 km), above and below the cloud tops (situated at 9.8 km height) at 17:00 UTC. The w field is represented a few minutes before the RO event (17:24 UTC).

200
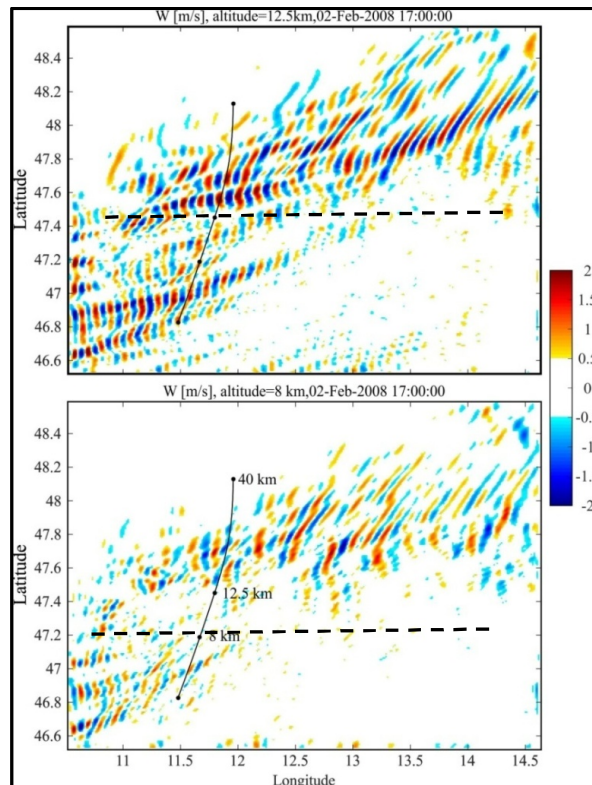
Figure 3: Simulated high resolution GW structures in the Alps region (defined in Fig. 1) for two altitude levels, above (upper panel) and below (lower panel) the cloud top. The line of tangent points corresponding to the collocated RO is indicated in both panels from lower (3 km) to upper (40 km) points.

205   The line of sight (dotted line) at both levels is also indicated.

The mesoscale outputs were obtained every 60 min. It is accepted that w adequately highlights the main GW amplitudes and wavelengths belonging to high and medium intrinsic frequency regimes. As it is known (e.g., de la Torre and Alexander, 1995; P. Alexander et al., 2008), a distortion is introduced in the measured GW λ_H and λ_Z by atmospheric soundings performed in any other than in vertical and horizontal

210 directions, as is the case during GPS RO events or during radiosoundings. In the case of RO events, it is known that a visibility condition imposed to the line of sight (LOS) described in P. Alexander et al. (2008) must be satisfied.The distortion is more or less significant, depending on the elevation angle of the sounding path and the GW aspect ratio (de la Torre et al., 2017, hereafter referred to as T17). For example, during vertically directed measurements with a single lidar, λ_H cannot be detected but λ_Z is not

215 distorted. Numerical simulations are not affected by this systematic error that affects current slanted atmospheric measurements. Below, we must distinguish between "apparent" and "real" λ_H and λ_Z values.

From WRF simulations, in Fig. 3, coherent mostly bi-dimensional GW structures with constant phase surfaces oriented along S-N direction and slightly tilted to N-E with increasing latitude, are noticed. The mean horizontal wind vector directed from NW to SE at 700 hPa, causing the forcing of mountain GW,

220 equals [3;-3] m/s at 18 UTC. Prevailing amplitudes and λ_H ranging between 1-2 m s^{-1} and 20-60 km, respectively, are distinguished. In this case study we observe in Fig. 3 that the quasi perpendicular orientation of the constant GW phases relative to the LOS ,clearly does not benefit the GW detection during the RO event (Alexander et al., 2008). The lower and upper altitudes of LTP are 3 km and 40 km, respectively. The observation of GW structures with short λ_H observed in Fig. 3 are expected to strongly

225 suffer from amplitude attenuation and should not be visible for GPS RO (Preusse et al., 2002; P. Alexander et al., 2008). Regarding the simulations, two main features may be remarked. GW amplitudes are weaker below than above the cloud tops and the structures are only partially stationary, when they are observed with increasing time steps during the convection development (not shown). These features suggest an expected two-folded contribution to the GW structures: one stationary, obviously of

230 orographic origin, and a second one associated to the convective source. This is confirmed below.

Taking into account the flexibility in any GW analysis due to their three-dimensional structure, in Fig. 4 we describe the zonal variation of w simulations, at representative UTC times and constant altitudes. A movie-like evolution of these structures (with a time step of 1 hour), reveals that to the west of 12°E, most of them are stationary, as expected from any orographic origin. Their amplitudes are more

235 significant early in the morning (Fig. 4a) and exhibit a general decrease with increasing local time. They reach again large amplitudes at stratospheric heights after a partial evanescence observed close to the tropopause, around 11 km height. The orographic structures are observed until the early afternoon (Fig. 4b). In Fig.4c, a suppression of the orographic structures is observed, probably associated to the unstable atmospheric conditions imposed during convection development. In Fig. 4d, non-stationary GW packets

240 between 12 km and 17 km height are generated by the convection development after mid-afternoon and radiated mainly above the cloud tops.The horizontal w profile corresponding to 15 km height is indicated in red for altitude reference. From the prevailing λ_H values between 20 km and 60 km, mentioned above in relation to Fig. 3, it appears that the shorter λ_H are of orographic origin and the longer λ_H are of convective origin.This can be confirmed by inspecting the time evolution of a Morlet Continuous Wavelet

245   Transform (CWT) corresponding to Figs. 4a, b and d, at altitude levels 12.5 km and 8 km, above and
        below the cloud top (located at 8.8 km) and latitude 47.3∘N (Fig. 5). Notice that the same GW main
        features may be seen both in w and in δT.
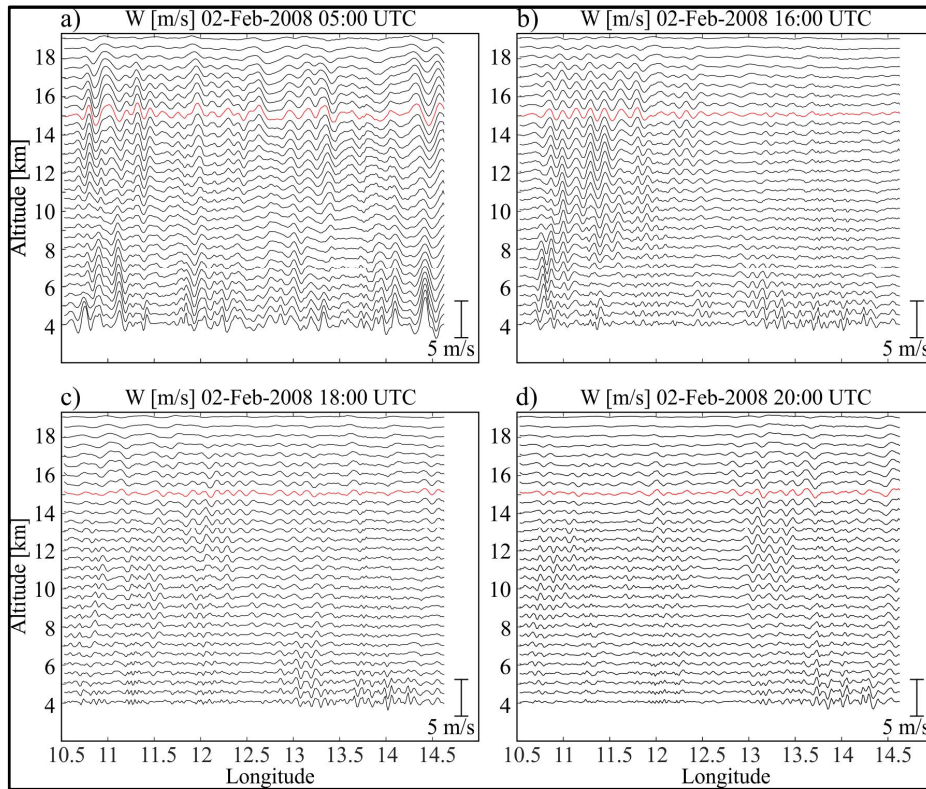
Figure 4: Zonal variation of w WRF simulations at representative times and constant altitudes in the Alps
250   region. The RO event took place between 11.9°E and 12.5°E, at 17:24 UTC (see Fig. 3). The red curve
        corresponds to the 15 km height.

        The CWT is a useful method to detect the main oscillation modes present in a signal analysis. As it is
        known, it is a powerful tool for studying multiscale and non-stationary processes occurring over finite
255   spatial and temporal domains (Lau and Weng, 1995). It allows detecting short-period as well as long-
        period oscillations. The CWT compares the original signal against a set of synthetical signals, which are
        called mother wavelets, obtaining correlation coefficients. These mother wavelets, together with a CWT
        and the discrete wavelet transform, define the theory of wavelets (Sang, 2013). The comparison between
        signals is carried out through a process of translation and contraction or dilation of the mother wavelet in
260   each signal portion. This process is repeated for all scales of mother wavelets, allowing the location of
        short life and high-frequency signals like sharp changes, thus obtaining detailed information. In this work,

the mother wavelet selected is the Morlet wavelet (Morlet, 1983), which consists of a flat wave modified by a Gaussian envelope.
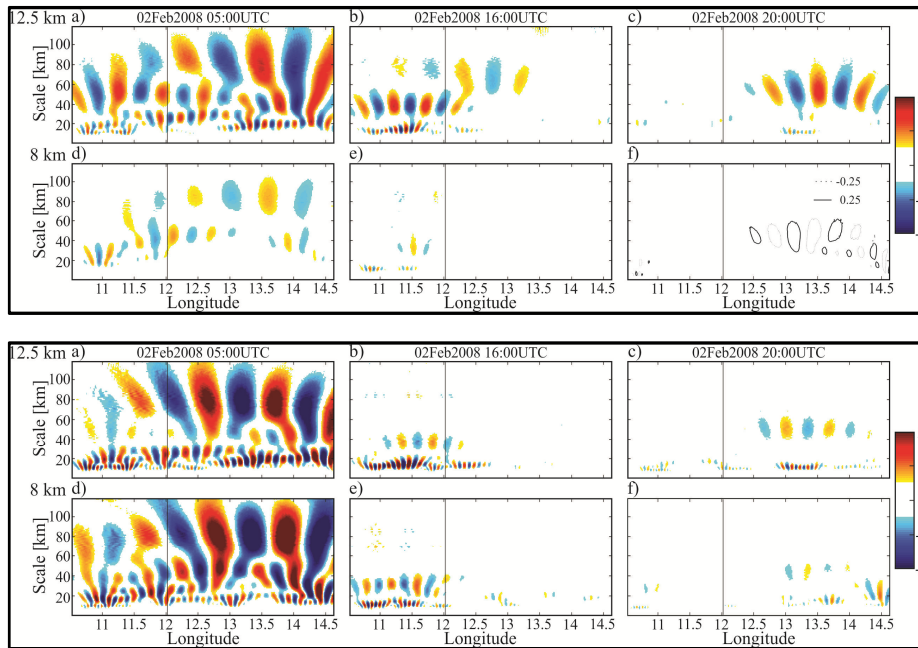
Figure 5: Continuous wavelet transform of w (upper panel) and of δT (lower panel) in the Alps region, corresponding to Fig. 4a, b, and d for latitude 47.3°N and altitudes 12.5 km and 8 km (above and below the cloud top located at 8.8 km).

In Fig. 3 and 4, λ_H at any altitude may be found by inspection of w as a function of latitude or longitude, and the zonal and meridional corresponding values, λ_x and λ_y, are thus obtained. This identification may be performed through any other dynamic or thermodynamic parameter, like T, pressure or density. These parameters reproduce (not shown) the GW features already observed, as well as the expected relative phase differences according to the polarization relations belonging to a high frequency GW. In the present case study, reliable values of λ_Z may be derived from Fig. 4, at any longitude and latitude. The applied procedure is simple. In the case of a clear orographic GW structure like the one observed on the left sector in Fig. 4a, we estimate the lateral displacement of any arbitrary identified phase minimum (or maximum), located at any longitude X_0 and altitude Z_0. The position of this extreme phase value is followed visually, with increasing height. After a vertical distance δZ, it is situated above the closest maximum (minimum) phase value at $Z_0 \pm \delta Z$. Then, the real value of λ_Z may be estimated as $\lambda_Z = 2\delta Z$. Taking into account the approximate nature of this procedure, we estimate λ_Z with a variability that depends on the selected initial altitude, latitude, and longitude. For example, from the orographic structures at lower levels in the western sector in Fig. 4a, the estimated value would be $\lambda_Z \approx 15$ km. In

addition to the lower (orographic) value $\lambda_H = 20$ km, a MW propagation angle $\psi = \tan^{-1}(\lambda_H/\lambda_Z) \approx 0.93$ rad

285 may be estimated.

3.1.2. *Analysis of gravity waves in the RO observation*

We analyze the wavelike structure of the RO T profile, shown at the center of Fig 2a, whose horizontally projected LTP is seen in Fig. 3.

290
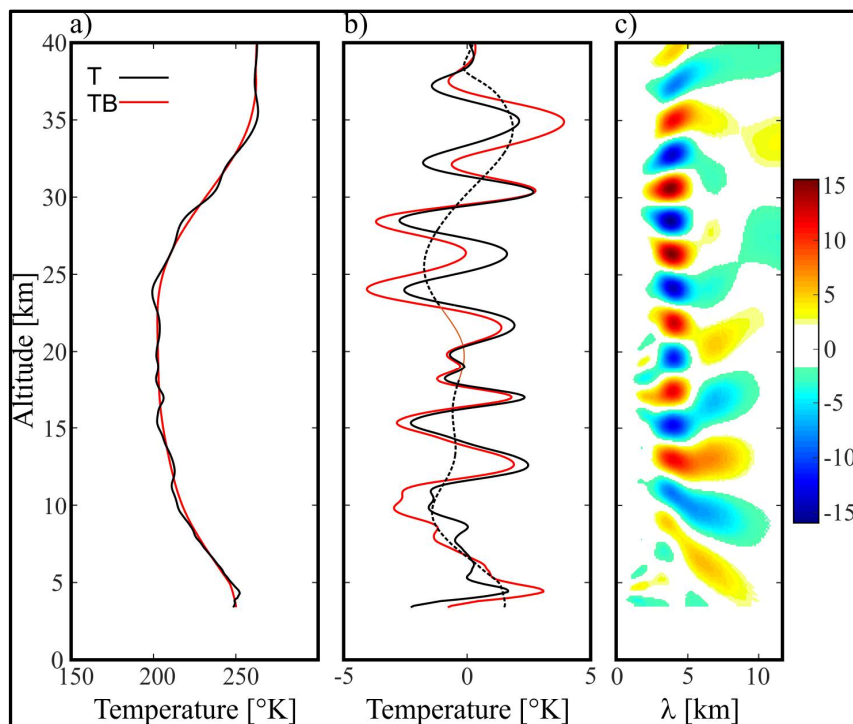
Figure 6: a) Retrieved RO T vertical profile (black line) and its corresponding low-pass background component TB (red line) in the Alps region. b) Remaining oscillation (black), isolated after applying a band-pass filter (red) and a double filtering process to the background (black dotted) profile. c)
295 Continuous wavelet transform (CWT) applied to the perturbation T structure, as a function of the vertical wavelength. The RO event took place at 17:24 UTC.

First, we remove the perturbation component of this single profile (Fig. 6a). If we try to apply a simple band-pass filter (e.g., de la Torre et al, 2006), as we did to calculate the CWT (see Fig. 5, lower panel),
300 we encounter the "tropopause problem", because RO T profiles are available as a function of altitude. In Fig. 5, we dealt with simulated T and w at constant Z as a function of longitude. As pointed out by Alexander et al. (2011), even if filters with ideal cut-offs existed, part of the problem would still be there

because the tropopause kink usually departs from a sinusoid or any other function that may be used as a basis. Real filters do not yield ideal spectral component isolations (side effects are amplitude reduction

305 for example) and may need some manual fine tuning procedures to optimize their performance. After a "perfect" band-pass is used, there should be no remaining components at wavelengths outside the considered range. Real filters behave differently, so using them more than once in a given way could a priori improve the removal of undesired wavelengths. This method has two steps: (i) we use the bandpass filtering to isolate the wavelength range of interest to separate the background and eliminate the noise,

310 and (ii) we perform a cutoff that is larger than or equal to the bandpass upper limit in order to remove large wavelengths representing background behavior or trends still present and to force a zero mean. We keep in mind that the tropopause kink in temperature can be viewed as the surrounding of a long sinusoidal peak. In the first step, we apply a bandpass between 1 km and 10 km, and in the second step, a cutoff of 10 km. The resulting filtered T profile is marked by the solid black line in Fig. 6b. A continuous

315 wavelet transform (CWT) is finally applied to the remaining T wave structure (Fig. 6c).

Fig. 6c shows a clear GW signal throughout the tropo-stratospheric region, with prevailing $\lambda_Z = 4$ km. A second considerably weaker mode is also present in the troposphere, with λ_Z close to 7 km. To search for a possible correspondence among these two modes and the structures observed in Figs. 3, 4 and 5, we know that when analyzing RO data, some care must be taken due mainly to the slanted nature of the

320 sounding, in addition to possible amplitude attenuation effects (P. Alexander et al., 2008; T17). In particular, for this RO event, the LOS stands at each TP almost exactly perpendicular to the GW phase surfaces observed in Fig. 3, at 88° from north direction (dotted lines in Fig. 3). This should prevent us to observe vertical oscillations corresponding to short λ_H structures as those seen in Fig. 3. In order to understand the meaning of the observed wavelike structures clearly observed in Fig. 6b, it is possible to

325 approximately reconstruct the RO vertical profile. This may be performed integrating along the LOS the simulated T field, centered at each TP. In doing so, we apply a weight Gaussian function along the LOS, centered at the TP. The statistical non symmetric contribution of wave activity along the LOS around each TP accounts for a net enhance or decrease of the background T, exhibiting the observed wavelike vertical profile for this RO event in Fig. 6b. In sum, this wavelike structure should be observed as the

330 result of an ensemble of GW contributions. It should not be confused with the presence of a possible prevailing monochromatic GW (see below, the Andes case study).

3.2. Study case for the Andes region

3.2.1. *Numerical simulations of gravity structures*

335 From the simulated dynamic and thermodynamic parameters, in Fig. 7 we show w for the Andes area (Fig. 1). It is shown at constant altitudes of 10 km and 16 km, above and below the cloud top (situated at 14 km height) at 17:00 UTC. The w field is represented a few minutes before the RO event (16:56 UTC). Coherent bi-dimensional GW structures with constant phase surfaces oriented from SW to NE are seen. The mean horizontal wind vector at 700 hPa directed from NW to SE is [7;-3] m/s at 18 UTC. It is known

340 that immediately to the south of this mountain region (de la Torre et al., 2015), close to the mountain tops,

two clearly different orographic GW structures may be systematically observed at constant pressure levels. One structure type shows highly elongated alternating positive and negative parallel *w* bands, aligned almost in N-S direction. The second type presents a bi-dimensional distribution too, but exhibits alternating fringes of much shorter longitude, mostly in SW–NE direction. The mean wind that forces the

345   MWs showing the 1D structures of the first type presents an intense zonal gradient of zonal wind, veering to an increasing westerly mean wind with increasing latitude. The meridional component is usually negligible. In the 2D structures of the second type, at and below mountain top levels, a prevailing intense negative meridional wind with less zonal wind contribution is observed. In the case study shown in Fig. 7, the mean wind at 700 hPa with a considerable negative meridional component should be associated to the

350   second type.
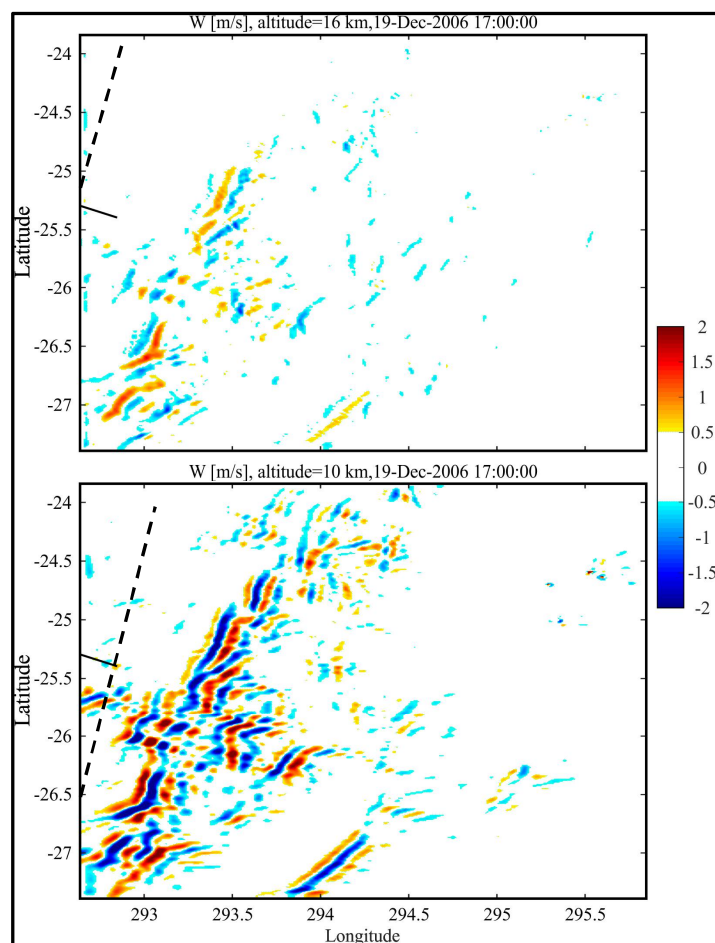
Figure 7: Simulated high resolution GW structures in the Andes region delimited in Fig. 1. Two constant altitudes, above (upper panel) and below (lower panel) the cloud tops, situated at 14 km. In this case, the mean LTP (black line) is located around 25.5°S and 67.1°W. The LTP altitudes corresponding to the

355   exteme inner and to the eastern edge are 5 and 22 km respectively.

In Fig. 8, we describe the zonal variation of w simulations, at representative UTC times and constant altitudes. As in the Alps case study, the waves observed are mostly stationary, foreseeably close to the highest Andes mountains, with tops close to 7 km height. The question here is to what extent the

360 convection development during the afternoon is able to generate GW in competition with the orographic source. The amplitudes are, inversely to what was observed at the Alps, less significant early in the morning and increase with local time until nighttime (Figs. 8a to c) according to the daily development of the subtropical jet. The presence of the jet above the mountains, with zonal component increasing with increasing height, suppresses possible critical layering effects. The general and sudden weakening of GW

365 amplitudes above the tropopause, situated at this region around 17 km, may be explained by the increase of the Scorer parameter (L^2). This parameter is directly (inversely) proportional to the buoyancy frequency (squared mean wind parallel to k_H). It is known that the horizontal wavelengths generated at mountain top levels, in the absence of horizontal density stratification, do not suffer variation with height. Then, wherever $L^2 < (2\pi/\lambda_H)^2$, the propagation is suppressed, as it happens where a strong mean wind is

370 present. This is observed in Fig. 8a to c. No clear variation of GW structures with time is observed above the convective development. The only slight phase displacement of the largest amplitudes to the east below the tropopause, observed in Fig. 8, could be reasonably attributed to the rapid time variation of the mean background wind. Intense amplitudes are observed at mountain top levels, with peak-to-peak values of 6 m s^{-1} and λ_H of 20 km. As it usually happens, the strongest or most excited wave scales with the

375 width of the ridge. A second main mode of around 40 km is seen in the corresponding CWT (Fig. 9) of w and δT, coinciding with previous observations performed close to mid-latitude Andes (de la Torre et al., 2011; 2015).
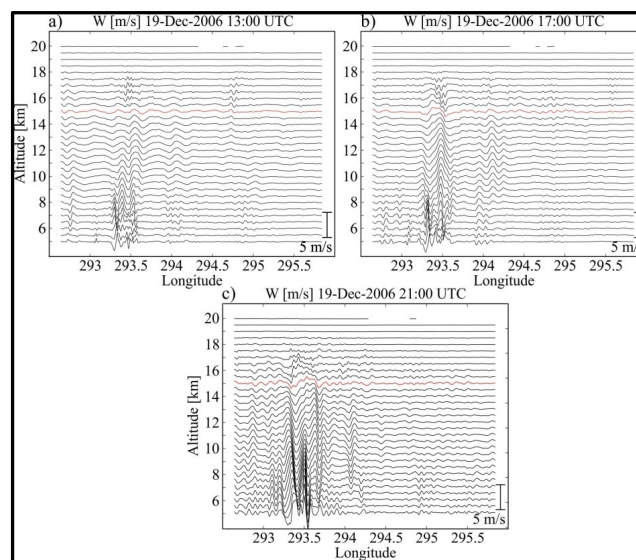
Figure 8. Zonal variation of w WRF simulations at representative times and constant altitudes in the
380 Andes region. The mean RO LTP is located at 25.5°S and 67.1°W and took place at 16:56 UTC.

Regarding λ_Z, in Fig. 8c, the eastwards phase displacement may be clearly noticed. It is estimated at approximately 20-25 km (as explained in Sect. 3.1.1). A corresponding GW propagation angle variation of the main mode, $\psi = \tan^{-1}(\lambda_H/\lambda_Z) \approx 0.93\text{-}1.02$ rad is estimated. This is a similar value to that observed in the Alps case study.

385
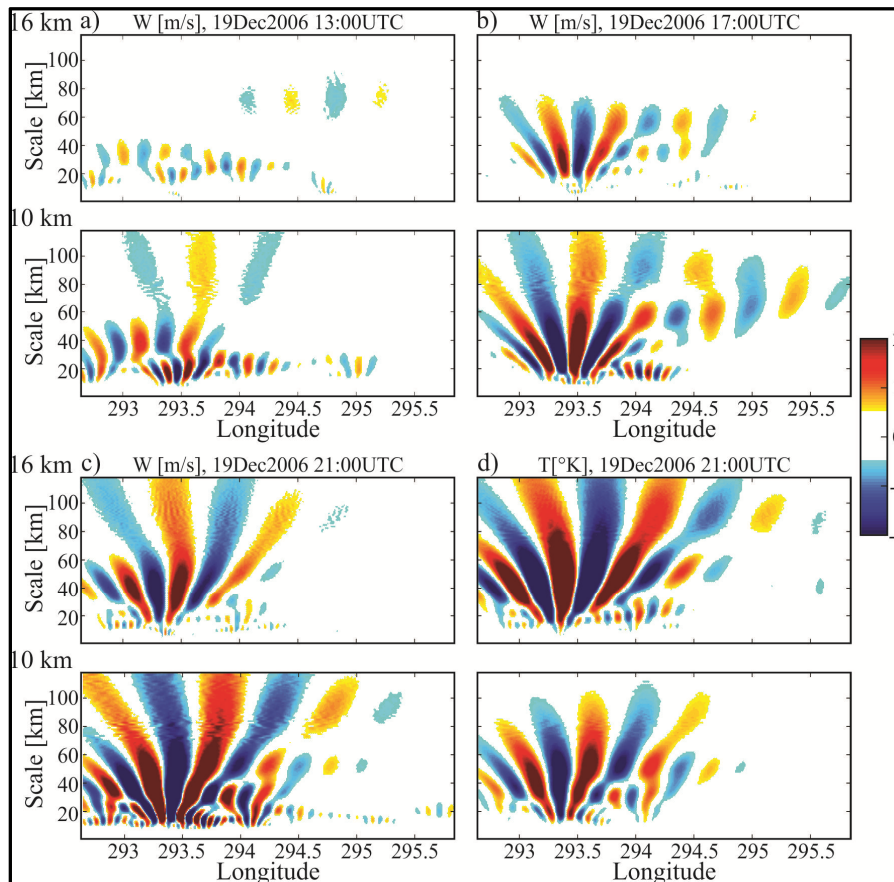
Figure 9: Continuous wavelet transform of w (a to c) and of δT (d) at representative times in the Andes region, corresponding to Figs. 8a, b and c at latitude 25.5°N and constant altitudes of 16 km and 10 km (above and below the cloud top located at 14 km).

390

3.2.2. *Analysis of gravity waves in the RO observation*

For this case study, we analyze the wavelike structure of the RO T profile already shown at the center of Fig 2a (lower panel), whose projected LTP is seen in Fig. 3 for case study 1. The procedure is identical to the one applied in case study 1.The utility of the double filter applied is more obvious here than in the

395   Alps case study. Also, the tropopause kink is sharper (Fig. 10 b). For this RO event, inversely to the

described situation in the Alps case study, the LOS stands at each TP almost aligned to the GW phase surfaces observed in Fig. 7, at 190° from north direction (dotted lines in Fig. 3). This should allow us to observe vertical oscillations in the RO profile corresponding to short λ_H structures seen in Fig. 7.
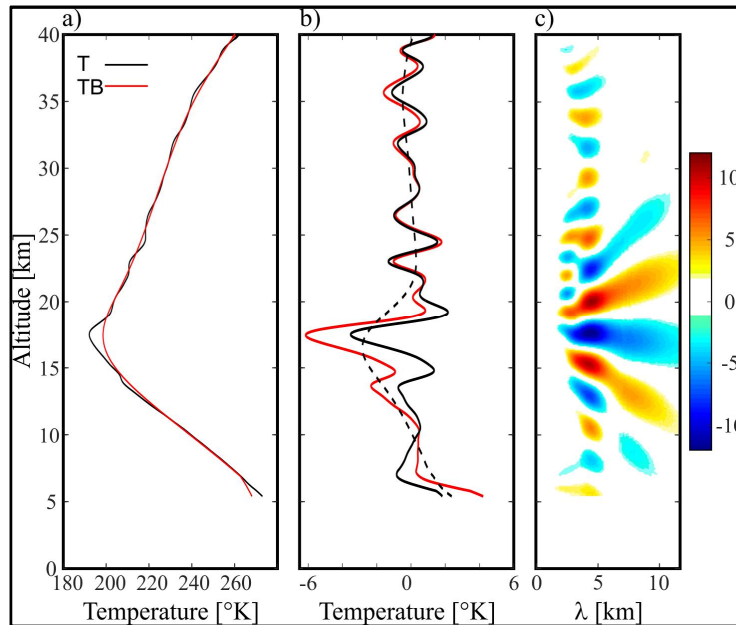
400   Figure 10: The same as in Fig. 6, for the case study in the Andes region.

In Fig. 10c, a clear GW signal appears also in the Andes case study, propagating throughout the tropo-stratospheric region with prevailing λ_Z = 4.5 km. Besides the obvious discrepancy observed also here between this measurement and the simulated λ_Z value (between 20 and 25 km height) , a non-negligible

405   signal at stratospheric heights still remains. This may be explained by the slanted region sounded by the LTP, which is different from the constant latitude vertical profiles shown in Fig. 8. The second main mode observed in the simulations is not obvious here. Nevertheless, a considerable underestimation of λ_Z is also present.

This discrepancy between measured and simulated λ_Z (an analogous discussion could be given regarding

410    $\lambda_{H,}$ too –see T17-) may be quantitatively explained as follows. It may be assumed that RO soundings yield T profiles almost instantaneously in such a way that GWs are "frozen" in space during the entire LTP retrieval. The vertical "real" and "apparent" (or measured) wavelengths (λ_z and λ_z^{ap}, respectively) are related according to the following expression (T17):

$$\lambda_Z^{ap} = \frac{\lambda_Z}{abs(1+\cot(\alpha)\cot(\psi))} \quad (1)$$

415   where α is the elevation angle, defined by a straight sounding path direction and the horizontal plane, and cot (ψ) is the ratio between the horizontal wavenumber vector ($\mathbf{k}_H$) projected on the vertical plane

containing LTP, and the vertical wavenumber k_Z. The ratio $k_H/k_Z = \lambda_Z/\lambda_H$ is also known as the GW aspect ratio, which was estimated to $\psi \approx 0.93$ rad (see Sect.3.1.1). We define the distortion as the ratio:

$$D = \frac{\lambda_Z^{ap}}{\lambda_Z} \quad (2)$$

420   and plot this parameter, following Eq. (1), as a function of α and ψ (red line in Fig. 11). For the LTP shown in Fig. 7, considering that both the horizontal and vertical excursion of LTP, as well as the upper and lower altitudes (40 and 3 km), are known, we infer an average $\alpha = 0.68$ rad. A different curve is obviously expected for different α values, althought fitting a similar shape. The divergence at high D values is only suggested by plotting its variability up to $D = 5$. The left green circle qualitatively indicates

425   the D-ψ GPS RO sector encompassing the functional relation among the 3 parameters. The right green circle is included, because an uncertainty beween α and $\pi-\alpha$ for our estimated aspect ratio still remains from our previous estimation. The white, light grey and grey backgrounds indicate, for reference purposes, the non-hydrostatic, hydrostatic non-rotating and hydrostatic rotating GW regimes, respectively. Both quadrants are separated by a vertical dashed curve. The horizontal dashed line

430   represents the non-distortion limit, where λ_Z and λ_Z^{ap} should coincide. According to both possibilities (the internal regions defined by any of the green circles), in the case considered (Fig. 10c), there are two possibilities indicating an under- and an overestimation of λ_Z respectively. This uncertainty can be removed by inspection of Fig. 10, were the underestimation is clearly seen. Then, the left circle is which properly represents the observed distortion of λ_Z from RO data in this case study.
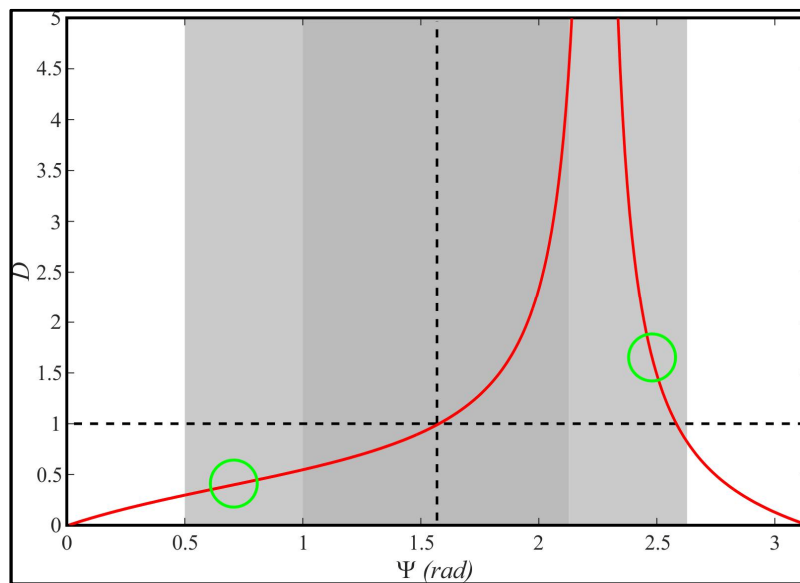
435

Figure 11: Distortion expected between measured and simulated λ_Z (green circles) regarding the GW parameters derived from the GPS RO event above the Andes, as detailed in Figs. 7 and 8. From both possible situations, only an under-estimation is expected (left green circle -see text).

440   The under- or overestimation of λ_Z and λ_H during RO measurements may have a considerable effect on a climatological calculation of the vertical flux of horizontal momentum asssociated to the GW activity, even if the α value corresponding to each RO, accounting for the slanted nature of the atmospheric sounding, is not properly considered.

445   **4. Conclusions**

The utility of GPS radio occultation (RO) observations for the investigation of convective systems and gravity waves (GW) over orographic regions in Europe and South America, respectively the Alps and Andes mountains, was investigated for an initial set of study cases. A collocation database was built between RO and cloud data over sub-tropical to mid-latitude regions for the selection of RO observations

450   in convective systems. We used RO bending angle and temperature profiles which were retrieved at the Wegener Center with processing version OPSv5.6. The storm systems were located in time and space according to the global deep convective tracking database ISCCP. From a set of 10 collocations between RO events and convection developments in the Alps and Andes regions, we analyzed gravity wave features derived from Weather Research and Forecasting (WRF) mesoscale model simulations and from

455   retrieved vertical RO temperature profiles. For this purpose, we focused on two representative case studies. Similar GW regimes and dominant vertical and horizontal wavelengths, from convective and orographic origin, are found in both regions. Mountain waves, the main gravity wave source in both regions, above the Alps reach higher altitudes than close to the Andes, as the background subtropical jet above this region seems to represent a constraint to the propagation of GW packets up to stratospheric

460   heights. This is related to to the decrease of the Scorer parameter in the absence of possible critical layers. Mountain waves are suppressed during convection development over the Alps. However, this is not observed over the Andes. The comparison between mesoscale simulations and measured vertical wavelengths of gravity waves,only here possible for the Andes case study), shows clear evidence of a considerable distortion affecting this parameter during the RO measurement.This distortion would affect

465   any calculation of momentum flux propagation due to GW generation, exclusively based on the information provided by the available RO temperature profiles. As explained in T17, GW distortions cannot be removed only from RO data, LTP and LOS information. We are actually studying the possibility to simultaneously calculate GW wavelengths and intrinsic frequencies only from measured relative phases among RO temperature profiles.

470

5 Data availability

The WEGC OPSv5.6 RO dataset is available on request from WEGC and will be made publicly available soon.Data on convective systems used in this study are available from the global deep convective tracking database of the International Satellite Cloud Climatology Project (ISCCP) via

475   <https://isccp.giss.nasa.gov/CT/>. Cloud data from METEOSAT are available from the EUMETSAT

processing centre via https://eoportal.eumetsat.int/userMgmt/login.faces and data from GOES are available from NOAA via https://www.class.ncdc.noaa.gov/saa/products/welcome.

Author contributions.

R. Hierro, A. de la Torre, A.K. Steiner, P. Alexander and P. Llamedo made the study design, performed the computational implementation and analysis, performed the numerical modelling, created the figures, and wrote the first draft of the paper.

A.K.Steiner provided guidance on RO data and analysis aspects and contributed to finalizing the manuscript.

P. Cremades provided recommendations and assistance in the WRF simulations.

Competing interests. The authors declare that they have no conflicts of interest.

Acknowledgements. We are grateful to R. Biondi (ISAC-CNR, Rome, Italy) for advice on cloud data and provision of the cloud detection algorithm and the reference climatology. We thank H. Truhetz (WEGC, Graz, AT) for help on WRF model aspects. We acknowledge UCAR/CDAAC (Boulder, CO, USA) for the provision of level 1a RO data and ECMWF (Reading, UK) for access to its analysis, and short-term forecast data. We thank the WEGC processing team members, especially M. Schwärz (WEGC, AT), for OPSv5.6 RO data and his special support. This study wasinitiated by the Programme of Exchange and Cooperation for International Studies between Europe and South America (PRECIOSA) by funding a research visit of R. Hierro at WEGC (University of Graz, Graz, AT). Part of the cooperation work wassupported by the Austrian Science Fund (FWF) under research grant P27724-NBL (VERTICLIM). The study has been supported by the CONICET under grants CONICET PIP11220120100034 and ANPCYT PICT 2013-1097.

References

Alexander, M. J.: The gravity wave response above deep convection in a squall line simulation, J. Atmos. Sci., 52, 2212–2226, 1995.

Alexander, P., de la Torre, A., Llamedo, P.: The interpretation of gravity waves signatures extracted from GPS radio occultations. *J. Geophys. Res.*, *113*, D16117, doi:10.1029/2007JD009390, 2008.

Alexander, P., de la Torre, A., Llamedo, P., Hierro, R., Schmidt, T., Haser, A., and Wickert., J.: A method to improve the determination of wave perturbations close to the tropopause by using a digital filter, Atmos. Meas. Tech., 4, 1777–1784, doi:10.5194/amt-4-1777-2011, 2011.

Angerer, B., Ladstädter, F., Scherllin-Pirscher, B., Schwärz, M., Steiner, A. K., Foelsche, U., and
510   Kirchengast, G.: Quality aspects of the Wegener Center Multi-Satellite GPS Radio Occultation Record
OPSv5.6, Atmos. Meas. Tech. Discuss., https://doi.org/10.5194/amt-2017-225, in review, 2017.

Barthlott, C., Corsmeier, U., Meißner, C., Braun, F., and Kottmeier, C.: The influence of mesoscale
circulation systems on triggering convective cells over complex terrain, Atmos. Res.,81, 150–175, 2006.
Beres, J. H., Alexander, M. J., and Holton, J. R.: Effects of tropospheric wind shear on the spectrum of
515   convectively generated gravity waves, J. Atmos. Sci., 59, 1805–1824, 2002.

Bica, B., Knabl, T., Steinacker, R., Ratheiser, M., Dorninger, M., Lotteraner, C., Schneider, S., Chimani,
B., Gepp, W., and Tschannett, S.: Thermally and Dynamically Induced Pressure Features over Complex
Terrain from High-Resolution Analyses, J. Appl. Meteor. Climatol., 46, 50–65, doi: 10.1175/JAM2418.1,
2007.

520   Biondi, R., Neubert, T., Syndergaard, S., and Nielsen, J. K.: Radio occultation bending angle anomalies
during tropical cyclones, Atmos. Meas. Tech., 4, 1053-1060, doi:10.5194/amt-4-1053-2011, 2011.

Biondi, R., Randel, W. J., Ho, S.-P., Neubert, T., and Syndergaard, S.: Thermal structure of intense
convective clouds derived from GPS radio occultations, Atmos. Chem. Phys., 12, 5309-5318,
https://doi.org/10.5194/acp-12-5309-2012, 2012.

525   Biondi, R., Steiner, A. K., Kirchengast, G., and Rieckh, T.: Characterization of thermal structure and
conditions for overshooting of tropical and extratropical cyclones with GPS radio occultation, Atmos.
Chem. Phys., 15, 5181-5193, doi:10.5194/acp-15-5181-2015, 2015.

Biondi, R., Steiner, A. K., Kirchengast, G., Brenot, H., and Rieckh, T.: Supporting the detection and
monitoring of volcanic clouds: a promising new application of Global Navigation Satellite System radio
530   occultation, Adv. Space Res., 60, in press. DOI:10.1016/j.asr.2017.06.039, 2017.

Clark, T. L., Hauf, T., and Kuettner, J. P.: Convectively forced internal gravity waves: Results from two-
dimensional numerical experiments, Q. J. R. Meteorol. Soc., 112, 899–925, doi:10.1002/qj.49711247402,
1986.

de la Torre A., Alexander, P., Llamedo, P., Menéndez, C., Schmidt, T., and Wickert, J.: Gravity waves
535   above andes detected from GPS radio occultation temperature profiles. II: jet mechanism?, Geophys. Res.
Lett, 33, L24810, doi:10.1029/2006GL027343, 2006.

de la Torre, A., Hierro, R., Llamedo, P., Rolla, A., and Alexander, P.: Severe hail storms near southern
andes   in   the   presence   of   mountain   waves,   Atmos.   Res.,   101,   (1-2),   112-
123,dx.doi.org/10.1016/j.atmosres.2011.01.015, 2011.

540   de la Torre, A., Alexander, P., Hierro, R., Llamedo, P., Rolla, A., Schmidt, T., and Wickert, J.: Large
amplitude gravity waves above the southern andes, the Drake passage and the Antarctic peninsula, J.
Geophys. Res. (Atmosphere), 117, D02106, dx.doi.org/10.1029/2011JD016377, 2012.

de la Torre, A., Pessano, H., Hierro, R., Santos, R., Llamedo P., and Alexander, P.: The influence of
topography on vertical velocity of air in relation to severe storms near the Southern Andes Mountains,
545   Atmos. Res., 156, 91-101, dx.doi.org/10.1016/j.atmosres.2014.12.020, 2015.

de la Torre, A., Alexander, P., Schmidt, T., Llamedo and P., Hierro, R.: On the distortions in calculated GW parameters during slanted atmospheric soundings, subm. to Atmos. Meas. Tech., 2017.

Demko, J. C., Geerts, B., Miao, Q., and Zehnder, J. A.: Boundary layer energy transport and cumulus development over a heated mountain, an observational study, Mon. Wea. Rev., 137, 447–468, 2009.

550 Dutta, G., Ajay Kumar, M. C., Vinay Kumar, P., Venkat Ratnam, M., Chandrashekar, M., Shibagaki, Y., Salauddin, M., and Basha, H. A.: Characteristics of high-frequency gravity waves generated by tropical deep convection: Case studies, J. Geophys. Res., 114, D18109, doi:10.1029/2008JD011332, 2009.

Evan, S., Alexander, M.J., and Dudhia, J.: Model Study of intermediate-scale tropical inertia-gravity waves and comparison to twp-ice campaign observations, J. Atmos. Sci., 69, 591–610, doi: 10.1175/JAS-555 D-11-051.1, 2012.

Fovell, R., Durran, D., and Holton, J. R.: Numerical simulations of convectively generated stratospheric gravity waves, J. Atmos. Sci., 49, 1427–1442, doi:10.1175/1520 0469(1992)049<1427:NSOCGS>2.0.CO;2, 1992.

Hierro, R., Pessano, H., Llamedo, P., de la Torre, A., Alexander, P., and Odiard, A.: Orographic effects 560 related to deep convection events over the Andes region, Atmos. Res., 120-121,216-225, dx.doi.org/10.1016/j.atmosres.2012.08.020, 2013.

Kursinski, E. R. and Gebhardt, T.: A method to deconvolve errors in GPS RO-derived water vapor histograms, J. Atmos. Oceanic Technol., 31 (12), 2606–2628, doi:10.1175/JTECH-D-13-00233.1, 2014.

Kursinski, E. R., Hajj, G. A., Schofield, J. T., Linfield, R. P., and Hardy, K. R.: Observing Earth's 565 atmosphere with radio occultation measurements using the Global Positioning System, J. Geophys. Res, 102(D19), 23429–23465, doi:10.1029/97JD01569, 1997.

Langhans, W., Schmidli, J., Fuhrer, O., Bieri, S., and Schär, C.: Long-Term Simulations of Thermally Driven Flows and Orographic Convection at Convection-Parameterizing and Cloud-Resolving Resolutions, J. Appl. Meteor. Climatol., 52, 1490–1510, doi:10.1175/JAMC-D-12-0167.1, 2013.

570 Lau, K.-M. and H. Weng: Climate signal detection using wavelet transform: How to make a time series sing, Bull. Am. Meteorol. Soc., 76, 2391–2402., 1995.

Preusse, P., Dornbrack, A., Eckermann, S.D., Riese, M., Schaeler, B., Bacmeister, J.T., Broutman, D. and Grossmann, K.U.: Space-based measurements of stratospheric mountain waves by CRISTA: 1. Sensitivity, analysis method, and a case study, J. Geophys. Res., 107(D23), 8178, 575 doi:10.1029/2001JD000699, 2002.

Morlet, J.: Sampling theory and wave propagation, in Acoustic Signal/Image Processing and Recognition, in NATO ASI, vol. 1, edited by C. Chen, 233–261, Springer-Verlag, New York., 1983.

Pandya, R. E. and Alexander, M. J.: Linear stratospheric gravity waves above convective thermal forcing, J. Atmos. Sci., 56, 2434–2446, 1999.

580   Rossow, W.B., Walker, A.W.,Beuschel D., and Roiter, M.: International Satellite Cloud Climatology Project (ISCCP) description of new cloud datasets. WMO/TD - No. 737, World Climate Research Programme (ICSU and WMO), Geneva, February 1996, pp. 115, 1996.

Röttger, J.: Structure and dynamics of the stratosphere and mesosphere revealed by VHF radar investigation, Pure Appl. Geophys., 118, 494–527, doi:10.1007/BF01586465., 1980.

585   Sang, Y.-F.: A review on the applications of wavelet transform in hydrology time series analysis, Atmos. Res., 122, 8–15,doi:10.1016/j.atmosres.2012.11.003., 2013.

Scherllin-Pirscher, B., Steiner, A. K., Kirchengast, G., Kuo, Y.-H., and Foelsche, U.: Empirical analysis and modeling of errors of atmospheric profiles from GPS radio occultation, Atmos. Meas. Tech., 4(9), 1875–1890, doi:10.5194/amt-4-1875-2011, 2011.

590   Scherllin-Pirscher, B., Steiner, A. K., Kirchengast, G., Schwärz, M., and Leroy, S. S.: The power of vertical geolocation of atmospheric profiles from GNSS radio occultation, J. Geophys. Res. Atmos., 2016JD025902, doi:10.1002/2016JD025902, 2017.

Schwärz, M., Kirchengast, G., Scherllin-Pirscher, B., Schwarz, J., Ladstädter, F., and Angerer, B.: Multi-mission validation by satellite radio occultation extension project—Final report, Tech. Rep. for
595   ESA/ESRIN No. 01/2016, Wegener Center, University of Graz, Graz, Austria. [online] Available from: https://wegcwww.uni-graz.at/publ/wegcpubl/arsclisys/2016/Schwaerz-etal_MMValRO FinRep_Dec2016.pdf, 2016.

Steiner, A. K. and Kirchengast, G.: Error analysis for GNSS radio occultation data based on ensembles of profiles from end-to-end simulations, J. Geophys. Res, 110(D15), D15307, doi:10.1029/2004JD005251,
600   2005.

Steiner, A. K., Hunt, D., Ho, S.-P., Kirchengast, G., Mannucci, A. J., Scherllin-Pirscher, B., Gleisner, H., von Engeln, A., Schmidt, T., Ao, C.,Leroy, S. S., Kursinski, E. R., Foelsche, U., Gorbunov, M., Heise, S., Kuo, Y.-H., Lauritsen, K. B., Marquardt, C., Rocken, C., Schreiner,W., Sokolovskiy, S., Syndergaard, S., and Wickert, J.: Quantification of structural uncertainty in climate data records from GPS radio
605   occultation, Atmos. Chem. Phys., 13, 1469–1484, doi:10.5194/acp-13-1469-2013, 2013.

Steiner, A. K., Lackner, B. C., Ladstädter, F., Scherllin-Pirscher, B., Foelsche, U., and Kirchengast, G.: GPS radio occultation for climate monitoring and change detection, Radio Sci., 46, RS0D24, doi:10.1029/2010RS004614, 2011.

Stephan, C. and Alexander, M. J.: Summer season squall-line simulations: sensitivity of gravity waves to
610   physics parametrization and implications for their parametrization in global climate models, J. Atmos. Sci., 71, 3376–3391, doi: 10.1175/JAS-D-13-0380.1., 2014.